

Many-body atomic response functions of xenon and germanium for leading-order sub-GeV dark matter-electron interactions in effective field theory

C.-P. Liu,^{1,*} Mukesh K. Pandey,^{2,1,†} Lakhwinder Singh,^{3,4} Chih-Pan Wu,^{1,5,‡}
Jiunn-Wei Chen,^{2,6,7,§} Hsin-Chang Chi,¹ and Henry T. Wong⁴

¹*Department of Physics, National Dong Hwa University, Shoufeng, Hualien 97401, Taiwan*

²*Department of Physics, Center for Theoretical Physics,
and Leung Center for Cosmology and Particle Astrophysics,
National Taiwan University, Taipei 10617, Taiwan*

³*Department of Physics, Central University of South Bihar, Gaya 824236, India*

⁴*Institute of Physics, Academia Sinica, Taipei 11529, Taiwan*

⁵*Département de physique, Université de Montréal, Montréal H3C 3J7, Canada*

⁶*Physics Division, National Center for Theoretical Sciences,
National Taiwan University, Taipei 10617, Taiwan*

⁷*Center for Gravitational Physics and Quantum Information,
Yukawa Institute for Theoretical Physics,
Kyoto University, Kyoto 606-8502, Japan*

Abstract

Direct searches of dark matter candidates with mass energies less than 1 GeV is an active research field. The energy depositions are comparable to the scale of atomic, molecular, or condensed matter systems, therefore many-body physics plays an important role in understanding the detector's response in dark matter scattering. We present in this work a comprehensive data set of atomic response functions for xenon and germanium with 12.2 and 80 eV energy thresholds, respectively, using the (multiconfiguration) relativistic random phase approximation. This approach takes into account the relativistic, exchange, and correlation effects in one self-consistent framework, and is benchmarked successfully by photoabsorption data from thresholds to 30 keV with $\lesssim 5\%$ errors. Comparisons with our previous and some other independent particle approaches in literature are made. It is also found that the spin-dependent (SD) response has significant difference from the spin-independent (SI) one such that the dark matter SD and SI interactions with electrons can be distinguished in unpolarized scattering, which is typical for direct search detectors. Finally, the exclusion limits set by current experiments are updated with our new results.

I. INTRODUCTION

Dark matter (DM) particles with masses smaller than GeV have been a subject receiving growing attention in recent years. They are well-motivated in theory, and their detection methods are within the reach of current and possible future experiments [1, 2]. Because of their small kinetic energies, $\lesssim O(\text{keV})$, direct detectors must have sub-keV energy thresholds, for which electron recoil (ER) is easier to be recorded than nuclear recoil. Among various mechanisms that can trigger ER signals, DM-impact ionization through DM-electron interactions is one of the most exploited search modes, and stringent exclusion limits have been set [3–26]

A key theory input for making an exclusion limit is the detector response functions, which lead to a prediction of the differential count rate at a detector with a prescribed DM interaction. As these low energy scales overlap with the ones of atomic, molecular, or even condensed-matter, many-body problems become an inevitable challenging task in

* cpliu@mail.ndhu.edu.tw

† mkpandey@gmail.com

‡ jpw750811@gmail.com

§ jwc@phys.ntu.edu.tw

constructing the relevant response functions. In this paper, we only focus on the kinematic regimes where detector responses can be well-described by the single-atom pictures.

There have been quite a few atomic calculations in literature that yield the response functions due to DM-electron interactions [3, 6, 10, 12, 15, 20, 25–30]. However, the discrepancies show that the predicted DM differential count rates depend sensitively on the underlying many-body approaches. While all works share a common ground at the mean field level, they differ on the formulations of the potentials used to compute the final scattered state: an atomic ion plus one free electron. Therefore, benchmarking an atomic many-body approach with some known processes is an important justification.

In our previous studies, we have successfully applied an *ab initio* method: (multi-configuration) relativistic random phase approximation [31, 32], (MC)RRPA, to photoionization of atomic (germanium) xenon and achieved excellent agreement with photoabsorption data. However, applying the same method to DM-impact ionization is both numerically challenging and intensive. Therefore, in our previous papers [10, 20], we resorted to a version of relativistic frozen core approximation (RFCA) for the final states, which does not include the exchange potential, nor electron-electron correlation beyond mean field. For selected energy transfers, we did perform (MC)RRPA calculations, and reported a general agreement at 20% except at low energies.

In this work, we overcome the numerical challenges. Consequently the resulting (MC)RRPA response functions of atomic xenon (germanium) would cover the full parameter space for direct sub-GeV DM searches with an energy threshold of 12.2 (80) eV. These atomic response functions incorporate not only the important ingredients being identified previously: relativistic correction [5, 10, 12, 20, 33] and exchange potential [28, 29], but furthermore, electron-electron correlation which is missing in previous treatments based on the independent particle picture. As will be shown in this paper, the correlation effect can be significant when scattering energy transfer is below 100 eV.

It is important to note that to analyze experiments using very-low-threshold germanium semiconductor detectors, one further needs condensed-matter many-body methods, for example, (most popularly) the density functional theory, in order to exhibit the band structures of the valence and conduction electrons and understand their response to DM scattering with a energy deposition $\lesssim 100$ eV (see, e.g., Refs. [34–36]). On the other hand, when energy deposition becomes large enough so that core electrons also get involved, their contributions

can be efficiently calculated by atomic methods, as these localized electrons are atomic-like. Our setting of 80 eV as the applicable energy threshold for germanium detectors is justified by benchmarking with photoabsorption data.

The paper is organized as follows. In Sec. II, we present the main results of this work: the atomic response functions of xenon and germanium by (MC)RRPA. Using photoabsorption data as benchmarks, we compare the (MC)RRPA and RFCA results, and show the substantial improvement of the former as a justification of (MC)RRPA. In Sec. III, we gather the essential formulae that are needed to compute the differential count rates based on the response function tables published along with the paper, and the codes that automatize the processes are also supplied. In Sec. IV, we compare and discuss the differences of the new (MC)RRPA results for DM-impact ionization from our previous RFCA and a few others. The exclusion plots of DM-electron interactions are updated with current experiment data sets, and we summarize the paper in Sec. V.

II. RESPONSE FUNCTIONS

A. Definition

Light dark matter, for its small kinetic energy, can trigger an observable electron recoil (ER) signal easier than a nuclear recoil (NR) signal, therefore, the detector response to the DM-electron (χ - e) interaction is our primary concern. From the conventional effective-field-theory construction [3, 37–45], the leading-order (LO) interaction Lagrangian

$$\begin{aligned} \mathcal{L}_{\chi-e}^{(\text{LO})} = & (c_1 + d_1/q^2) (\chi^\dagger \mathbb{1}_\chi \chi) \cdot (e^\dagger \mathbb{1}_e e) \\ & + (c_4 + d_4/q^2) (\chi^\dagger \vec{S}_\chi \chi) \cdot (e^\dagger \vec{S}_e e) , \end{aligned} \quad (1)$$

contains a spin-independent (SI) and a spin-dependent (SD) parts, where $\mathbb{1}_{e(\chi)}$ and $\vec{S}_{e(\chi)}$ are the unity and spin operators for the electron (DM) field, respectively. The constants c_1 and c_4 denote the strengths for the short-ranged interaction terms, while d_1 and d_4 for the long-ranged counterparts where q is the magnitude of the 3-momentum transfer.

For a complex atom with Z electrons, the possible atomic transitions are governed by four transition operators in coordinate space:

$$\mathbb{1}_e \rightarrow \sum_{i=1}^Z e^{i\vec{q}\cdot\vec{r}_i} \mathbb{1}_i, \quad \vec{S}_e \rightarrow \sum_{i=1}^Z e^{i\vec{q}\cdot\vec{r}_i} \frac{\vec{\sigma}_i}{2}.$$

The 2×2 unity and Pauli matrices, $\mathbb{1}_i$ and $\vec{\sigma}_i$, act on the nonrelativistic wave function of the i th electron. To take into account the relativistic corrections, they are replaced by $\mathbb{1}_i^{\text{D}} = \begin{pmatrix} \mathbb{1}_i & 0 \\ 0 & \mathbb{1}_i \end{pmatrix}$ and $\vec{\sigma}_i^{\text{D}} = \begin{pmatrix} \vec{\sigma}_i & 0 \\ 0 & \vec{\sigma}_i \end{pmatrix}$ when atomic wave functions are in a Dirac 4-spinor form.

While Cartesian operators look compact in form, for actual atomic many-body calculations, it is advantageous to transform them into spherical multipoles. They are

$$\hat{C}_J^{M_J}(q) = \sum_{i=1}^Z j_J(qr_i) Y_J^{M_J}(\Omega_{r_i}) \mathbb{1}_i^{\text{D}}, \quad (2a)$$

$$\hat{\Sigma}_J^{M_J}(q) = \sum_{i=1}^Z j_J(qr_i) \vec{Y}_{JJ}^{M_J}(\Omega_{r_i}) \cdot \vec{\sigma}_i^{\text{D}}, \quad (2b)$$

$$\begin{aligned} \hat{\Sigma}'_J^{M_J}(q) = \sum_{i=1}^Z \left\{ -\sqrt{\frac{J}{2J+1}} j_{J+1}(qr_i) \vec{Y}_{JJ+1}^{M_J}(\Omega_{r_i}) \right. \\ \left. + \sqrt{\frac{J+1}{2J+1}} j_{J-1}(qr_i) \vec{Y}_{JJ-1}^{M_J}(\Omega_{r_i}) \right\} \cdot \vec{\sigma}_i^{\text{D}}, \end{aligned} \quad (2c)$$

$$\begin{aligned} \hat{\Sigma}''_J^{M_J}(q) = \sum_{i=1}^Z \left\{ \sqrt{\frac{J+1}{2J+1}} j_{J+1}(qr_i) \vec{Y}_{JJ+1}^{M_J}(\Omega_{r_i}) \right. \\ \left. + \sqrt{\frac{J}{2J+1}} j_{J-1}(qr_i) \vec{Y}_{JJ-1}^{M_J}(\Omega_{r_i}) \right\} \cdot \vec{\sigma}_i^{\text{D}}, \end{aligned} \quad (2d)$$

where $j_J(qr)$ is the spherical Bessel function, $Y_J^{M_J}(\Omega_r)$ the spherical harmonics of solid angle Ω_r , and $\vec{Y}_{JL}^{M_J}(\Omega_r)$ the vector spherical harmonics formed by recoupling of $Y_L^{M_L}(\Omega_r)$ and the unit vector \hat{r} , whose spherical projection is proportional to Y_1^λ .¹

When the atomic initial state is unpolarized and the final polarization state is not detected (i.e., summed), the algebra on the total magnetic quantum numbers can be greatly simplified. In combination with total angular momentum and parity selection rules, there is no interference from the scattering amplitudes of these four multipole operators. Therefore, we define four distinct atomic response functions

$$\begin{aligned} \mathcal{R}_{O_J}(T, q) = \sum_{F J_F} \overline{\sum_{I J_I}} \left| \langle F, J_F \parallel \hat{O}_J(q) \parallel I, J_I \rangle \right|^2 \\ \times \delta(E_{\mathcal{F}} - E_{\mathcal{I}} - T), \end{aligned} \quad (3)$$

¹ For these multipole operators and their corresponding response functions, we use the same convention as Refs. [38, 46].

with \hat{O}_J being one of $(\hat{C}_J, \hat{\Sigma}_J, \hat{\Sigma}'_J, \hat{\Sigma}''_J)$. The atomic initial (final) state $|\mathcal{I}(\mathcal{F})\rangle$ is completely specified by its total angular momentum and z -projection, $J_{I(F)}$ and $M_{J_{I(F)}}$, and other quantum numbers collectively labeled by $I(F)$. The double-bared, or reduced, matrix element notation and the missing of $M_{J, J_{I(F)}}$ indicate the reduction of angular momentum algebra. The bar over the initial state sum means the average of the ground state configurations. The delta function imposes the energy conservation: T is the energy deposition by the DM particle which causes the ionization of a bound electron, plus a tiny atomic center-of-mass recoil: $q^2/(2m_A)$ where m_A is the atomic mass. For a non-relativistic incident DM particle, the atomic recoil is only important at high energy transfers which also require high momentum transfers. After the sum and average is completed, one clearly sees the response function only depends on two variables: the energy and momentum transfer by DM.

B. (MC)RRPA and RFCA Results

In this work, the atomic initial, i.e., ground, state $|I, J_I M_{J_I}\rangle$ is obtained by solving the Dirac-Fock (DF) equation for closed-shell atoms like xenon. For open-shell atoms like germanium, an additional feature, the multiconfiguration (MC) of the reference state, is implemented that yields the MCDF equation. The atomic final, i.e., ionized, state $|F, J_F M_{J_F}\rangle$, is obtained by solving the corresponding relativistic random phase approximation (RRPA) equation for xenon, and the MCRRPA equation for germanium, respectively. Compared with our previous works [10, 20] that used RFCA ² for the final state, the (MC)RRPA approach, ³ while being much more time-consuming, is not only self-consistent with the exchange term built in, but also includes electron-electron correlation beyond mean field through RPA. Details of (MC)RRPA can be found in, e.g., Refs. [31, 32]. In Appendix, we give an outline of how the wave functions and transition amplitudes are computed in the (MC)RRPA scheme.

² In Refs. [10, 20], we used the acronym FCA for the method. Here we add an adjective “relativistic” to better characterize it and make distinction from the corresponding nonrelativistic version.

³ The abbreviation (MC)RRPA refers to RRPA for closed-shell and MCRRPA for open-shell atoms, respectively.

1. Photoabsorption benchmark

Many-body correlation, which is beyond typical mean-field type approaches, has been known to play an important role in proper understanding of excited states of a many-body system. For an atom system, its photoabsorption cross section, which is dominated by photoelectron emission in the energy range of 10 eV to 100 keV, provides an ideal testing ground.

In radiation gauge, the photoabsorption process goes through two types of vector current multipole operators, transverse electric, \hat{E}_J^{MJ} , and transverse magnetic \hat{M}_J^{MJ} :

$$\hat{E}_J^{MJ}(q) = \sum_{i=1}^Z \frac{1}{q} \vec{\nabla}_i \times [j_J(qr_i) \vec{Y}_{JJ}^{MJ}(\Omega_{r_i})] \cdot \vec{\zeta}_i^{\mathcal{D}}, \quad (4a)$$

$$\hat{M}_J^{MJ}(q) = \sum_{i=1}^Z j_J(qr_i) \vec{Y}_{JJ}^{MJ}(\Omega_{r_i}) \cdot \vec{\zeta}_i^{\mathcal{D}}, \quad (4b)$$

where $\vec{\zeta}_i^{\mathcal{D}} = \begin{pmatrix} 0 & \vec{\sigma}_i \\ \vec{\sigma}_i & 0 \end{pmatrix}$. In terms of their corresponding response functions \mathcal{R}_{E_J} and \mathcal{R}_{M_J} , the total cross section of absorbing a photon of energy T is given by the relation

$$\sigma_{\text{abs}}^{(\gamma)}(T) = \frac{2\pi^2\alpha}{T} \mathcal{R}_{\perp}^{(\gamma)}(T, q = T), \quad (5)$$

$$\mathcal{R}_{\perp}^{(\gamma)}(T, q) = \frac{4\pi}{2J_I + 1} \sum_{J \geq 1}^{\infty} [\mathcal{R}_{E_J}(T, q) + \mathcal{R}_{M_J}(T, q)]. \quad (6)$$

The symbol “ \perp ” of \mathcal{R}_{\perp} denotes the transverse character of the associated response function, and because the photon is real, only the on-shell part of the response function $q = T$ is probed by photoabsorption.

In the left panel of Fig. 1, we show the comparison of our RRPA and RFCA results for xenon with experimental data compiled from Refs. [47–50]. In our new RRPA run, we overcome several numerical difficulties in the energy range of 70-90 eV. As a result, we improve on our previous RRPA calculations reported in Ref. [51] such that the new RRPA calculations pass the benchmark in the entire energy range from threshold up to 30 keV. Except when T is near the photoabsorption edges, i.e., ionization thresholds, the general agreement between RRPA and experiments is within 5%. An even more important feature shown in this figure is the comparison between the RRPA and RFCA results. While

RFCA agrees with experiments well for $T \gtrsim 1$ keV, for lower energies, there are noticeable discrepancies.

The range between 70 eV to 1 keV was an important testing ground for atomic calculations historically. It was Copper who first proposed a qualitative solution using a simple central field potential for the $4d$ electrons [52], whose ionizations dominate the cross section. While later approaches such as refined central potential [53] and Hartree-Fock approximation [54] yield better agreements, they failed to describe correctly the shapes of the two peaks and the positions of two maxima (one at 100 and the other at 291eV) and one minimum (193 eV), due to the missing of correlation effect. Similarly for $T < 70$ eV, the correlation effect is also important for the ionization of $5p$ and $5s$ orbitals and was first demonstrated in Ref. [55] by applying RRPA to a limited subshells including $5p$, $5s$, and $4d$. With modern computing resources, the valence electron configuration in our RRPA run includes all except two innermost $1s$ electrons, whose high ionization energy, ~ 35 keV, justify their inert character in low energy processes. This excellent benchmark not only justifies the robustness of our approaches, but also indicate the necessity of a genuinely many-body response function for xenon detector at the energy range of sub-keV.

In the right panel of Fig. 1, the comparison of our MCRRPA results for germanium (all electrons including $1s$ are treated as valence) with experimental data compiled from Ref. [47] is essentially the same as reported in Ref. [56]. Except in $T \lesssim 80$ eV, where our single-atom calculation misses the crystal band structures of $3d$, $4s$, and $4p$ orbitals, the inner core states of germanium semiconductor are highly localized and their dynamics in photoionization can be accurately described by MCRRPA. As a result, we only provide response functions for germanium for $T \geq 80$ eV. On the other hand, the discrepancy between RFCA and MCRRPA shown in this figure for $T \lesssim 40$ eV gives another indication that correlation is important for outer shell electrons including $3d$, $4s$, and $4p$ for atomic germanium.

2. Data tables and parameter space covered

Four types of atomic response functions: charge (C), axial longitudinal (L^5), axial transverse electric (E^5), and axial transverse magnetic (M^5), $\mathcal{R}_{C,L^5,E^5,M^5}(T, q)$, which correspond to transition operators \hat{M} , $\hat{\Sigma}''$, $\hat{\Sigma}'$, $\hat{\Sigma}$, respectively, are compiled in this work. The digital

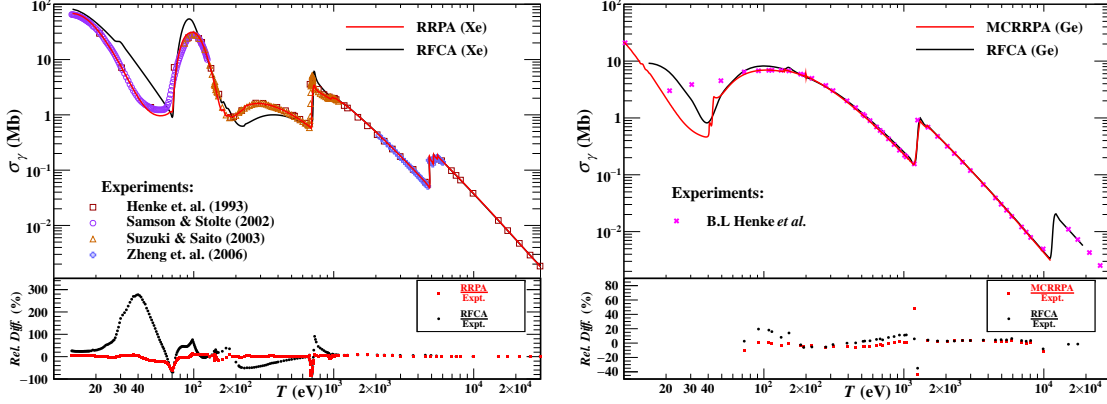


Figure 1. The photoabsorption cross sections of xenon (left) and germanium (right) are shown. The solid red and black lines indicate the results of our (MC)RRPA and RFCA calculations, respectively. The germanium results are compared with Ref. [47], and the xenon results are compared with Refs. [47–50]. The percentage differences of (MC)RRPA and RFCA calculations from the experimental data are shown in bottom insets.

data files are shipped along with the codes that supplement this paper. An excerpt from the charge response function of xenon is reproduced in Table I. The first and the second column give the DM energy and momentum transfer, T and q in units of eV. The third column gives the RRPA value in units of $1/\text{eV}$. The RFCA response functions are also provided for reference, and their corresponding values are listed in the fourth column.

The minimal values of T for xenon and germanium are fixed at $T_{\min} = 12.2$ and 80 eV, respectively. The former is the first ionization energy of xenon, and the latter is the lower limit that atomic calculation can be safely applied to semiconductor germanium. The maximal value of T is fixed at $T_{\max} \approx 5$ keV, which is roughly the largest kinetic energy of a one-GeV DM particle in our galaxy.

The main reason why a (MC)RRPA calculation is much more time-consuming than typical independent-particle ones is the evaluation of the matrix element of $\hat{O}_J(q)$. For each operator of a specific q and J , a (MC)RRPA equation is set up and needs to be solved self-consistently. As a result, the momentum grid and the multipole expansion have to be fixed economically.

For a given T , the momentum grid is determined based on the following considerations. By the kinematics of galactic cold DM, the minimal and maximal momentum transfer for a

T (eV)	q (eV)	$\mathcal{R}_C^{(\text{RRPA})}(\text{eV}^{-1})$	$\mathcal{R}_C^{(\text{RFCA})}(\text{eV}^{-1})$
12.2	4713.228991	3.147887e-02	4.145701e-02
12.2	5577.051911	2.974885e-02	3.153066e-02
12.2	6440.874832	2.225311e-02	2.174820e-02
12.2	7304.697752	1.377670e-02	1.282298e-02
12.2	8168.520673	7.319998e-03	6.346181e-03
12.2	9032.343593	3.417749e-03	2.556397e-03
12.2	9896.166514	1.441683e-03	7.762880e-04
12.2	10759.989434	5.939323e-04	1.618018e-04
12.2	11623.812355	2.890757e-04	7.420893e-05
12.2	12487.635275	1.943690e-04	1.456781e-04
\vdots	\vdots	\vdots	\vdots

Table I. Excerpt from the data files for the charge response function of xenon, calculated by the RRPA (3rd column) and RFCA (4th column) methods.

given speed v_χ are simply

$$q_{\min}^{\max} = m_\chi v_\chi (1 \pm \sqrt{1 - T/(T_\chi)}),$$

respectively, where $T_\chi = \frac{1}{2}m_\chi v_\chi^2$ is the NR kinetic energy of the DM particle. Given that v_{\max} is the maximum DM speed without escaping our galaxy, a m_χ independent absolute threshold value can be fixed by $q_{\text{th}} = T/v_{\max}$. The maximum momentum transfer which can be handled reliably by our current (MC)RRPA codes is 2.5 MeV. Because of the fast convergence in radial integrals involving the spherical Bessel function of increasing q , the momentum grid has a denser sampling at the low q region, and the high momentum tail beyond 2.5 MeV is extrapolated to the end point $q_{\text{end}} = \sqrt{2m_A(T - T_{\min})}$.

The multipole expansion is truncated at J_{\max} where its contribution is on the order of 10^{-4} compared to the biggest one in the series. For the current coverage of (T, q) , we found that $J_{\max} \leq 6$ is sufficient. This is supported by our RFCA calculations which can easily handle high multipoles.

In Figs. 2 and 3, the four response functions \mathcal{R}_C , \mathcal{R}_{L^5} , \mathcal{R}_{E^5} , and \mathcal{R}_{M^5} for xenon and germanium, respectively, are plotted in two dimensional planes of T and q with color gradients

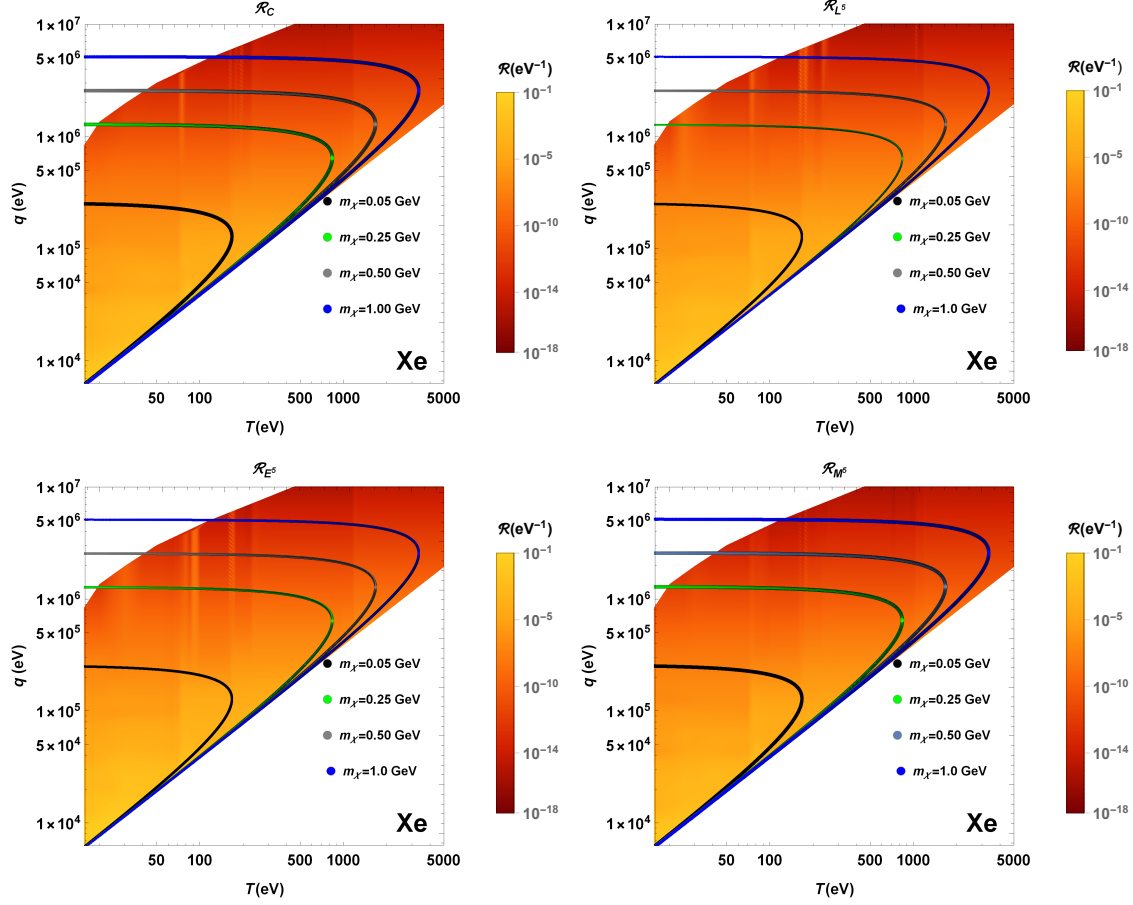


Figure 2. Four atomic responses \mathcal{R}_C , \mathcal{R}_{L^5} , \mathcal{R}_{E^5} , and \mathcal{R}_{M^5} of xenon as functions of T and q calculated by RRPA with values shown by color gradients

showing their magnitudes. There are two kinetically forbidden regions: the lower right is to guarantee a large enough q for an energy transfer T , i.e., q_{th} defined above. The upper left is to cut off an atomic recoil $q^2/2m_A$ too large to leave sufficient energy left for first ionization E_{ion} . The four contours bound the allowed energy transfer, $T \in [0, 1/2m_\chi v_{\text{max}}^2]$, and momentum transfer, $q \in [q_{\text{min}}, q_{\text{max}}]$ depending on T with $v_\chi = v_{\text{max}}$, by scattering of four different dark matter masses. As can be seen, the current data tables are sufficient to cover dark matter searches with masses up to ~ 1 GeV, and lower to ~ 10 (80) MeV for xenon (germanium) detectors.

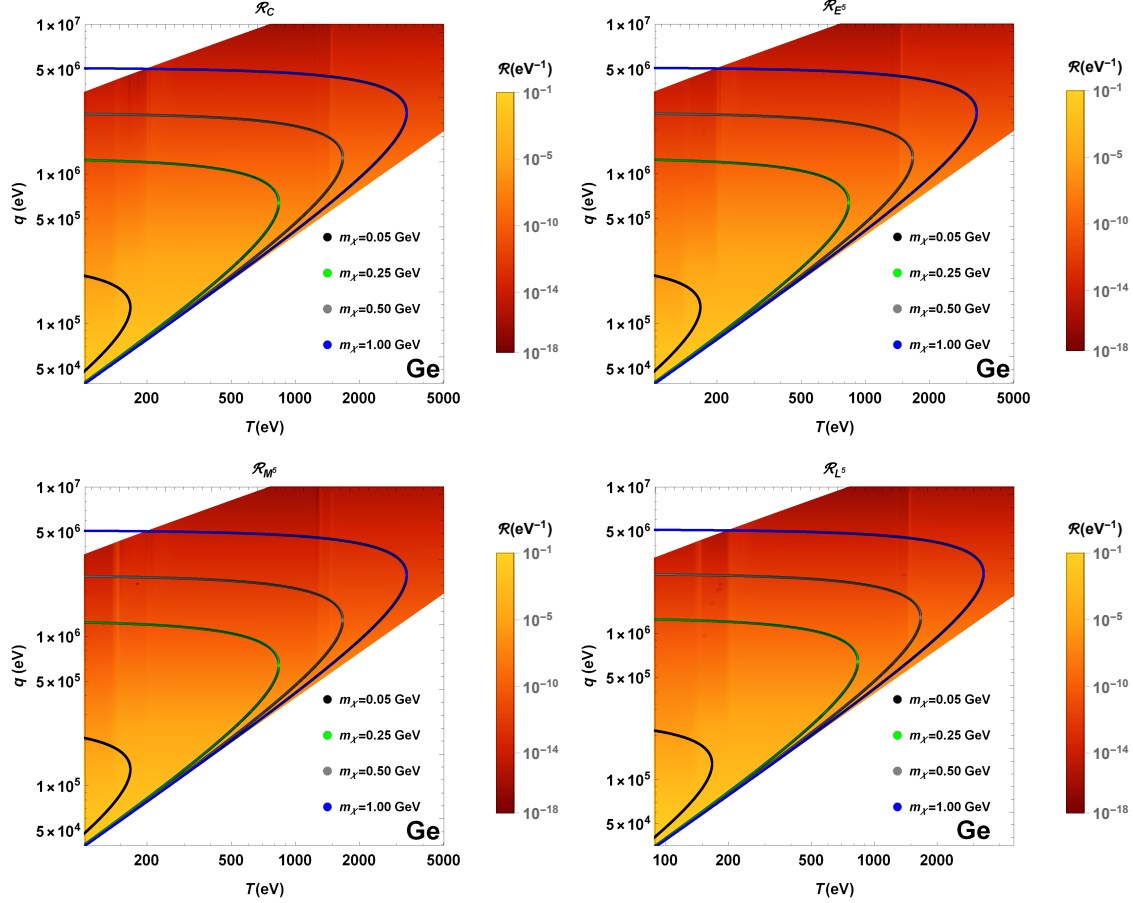


Figure 3. Four atomic responses \mathcal{R}_C , \mathcal{R}_{L^5} , \mathcal{R}_{E^5} , and \mathcal{R}_{M^5} of germanium as functions of T and q calculated by MCRIPA with values shown by color gradients.

III. DIFFERENTIAL CROSS SECTIONS AND RATES

A. Formulation

With the relevant response functions being obtained, it is straightforward to assemble them and calculate differential cross sections and rates. Here we outline the general procedure and essential formulae.

The differential cross section due to the LO χ - e interaction for a DM particle of mass m_χ and speed v_χ is calculated by an integration over momentum transfer q

$$\frac{d\sigma}{dT} = \frac{1}{2\pi v_\chi^2} \int_{q_{\min}}^{q_{\max}} q dq \left\{ (c_1 + d_1/q^2)^2 \mathcal{R}_{\text{SI}}(T, q) + (\bar{c}_4 + \bar{d}_4/q^2)^2 \mathcal{R}_{\text{SD}}(T, q) \right\}, \quad (7)$$

where $(\bar{c}_4, \bar{d}_4) = \sqrt{s_\chi(s_\chi + 1)/12}(c_4, d_4)$ with s_χ being the spin of the DM particle. The SI

and SD response functions are obtained by

$$\mathcal{R}_{\text{SI}}(T, q) = \frac{4\pi}{2J_I + 1} \sum_{J=0} \mathcal{R}_{C_J}(T, q), \quad (8a)$$

$$\mathcal{R}_{\text{SD}}(T, q) = \frac{4\pi}{2J_I + 1} \left\{ \sum_{J=1} \left[\mathcal{R}_{E_J^{\text{S}}}(T, q) + \mathcal{R}_{M_J^{\text{S}}}(T, q) \right] + \sum_{J=0} \mathcal{R}_{L_J^{\text{S}}}(T, q) \right\}. \quad (8b)$$

From the differential cross section for a fixed DM speed v_χ , the differential count rate per single atom is computed by convoluting with the DM number flux spectrum

$$\frac{dR}{dT} = n_\chi \int d^3v_\chi f(\vec{v}_\chi) v_\chi \frac{d\sigma}{dT}, \quad (9)$$

where n_χ is the total galactic DM number density, and $f(\vec{v}_\chi)$ is the three-dimensional DM velocity distribution with respect to the Earth frame. The seasonal effect, which is due to the relative Earth velocity to the local DM halo, \vec{v}_E , is built in $f(\vec{v}_\chi)$.

The advantages of using response functions can now be seen more clearly. In the whole process of predicting a DM-atom ionization rate, the inputs include (i) the DM spectrum from astrophysics and cosmology, (ii) the DM-electron interaction from particle physics, and (iii) high-quality wave functions from atomic physics. By packing up the most computing-expensive part (iii) of the inputs in the form of response functions, the studies of parts (i) and (ii) can be carried out using the same atomic input.

B. Accompanied Code and Test Examples

We supply computer codes, in both C and Mathematica, along with this paper that read in the database of response functions and compute the differential count rate in units of $\text{kg}^{-1}\text{keV}^{-1}\text{day}^{-1}$ through either the SI or SD χ - e interaction at leading order.⁴ For local DM velocity spectrum $f(\vec{v}_\chi)$, we assume the Maxwellian form of the standard halo model (see, e.g., Ref. [57]) in this paper, with seasonal modulation averaged out. For all numerical results, the local DM density ρ_χ , circular speed v_0 , escape speed v_{esc} , and Earth speed v_E

⁴ The code and data tables can be downloaded through the link: <https://web.phys.ntu.edu.tw/~jwc/DarkMatterandNeutrinoGroup/index.html?pg=AtomicResponses>.

are chosen to be 0.4 GeV/cm^3 , 220, 544, and 232 km/s, respectively. For the test examples, we further fix $m_\chi = 1 \text{ GeV}$, and the χ - e coupling constants for the SR and LR interactions to be $c_1 = \bar{c}_4 = 1 \text{ GeV}^{-2}$ and $d_1 = \bar{d}_4 = 10^{-9}$, respectively.

Note that the above computations involve a double integration, first over q and second over v_χ (when the seasonal effect is averaged). We can easily compare them with a commonly-used procedure which reverses the integration order and assume the only v_χ dependence of $d\sigma/dT$ is $1/v_\chi^2$. This results in the so-called mean inverse speed function

$$\eta(\tilde{v}_{\min}) = \int d^3v_\chi f(\vec{v}_\chi) \frac{1}{v_\chi} \Theta(v_\chi - \tilde{v}_{\min}), \quad (10)$$

which only integrates the DM velocity spectrum above a minimal value

$$\tilde{v}_{\min} = \frac{T}{q} + \frac{q}{2m_\chi},$$

that can afford a given energy and momentum transfer at T and q . By this ansatz, the differential rate can alternatively be computed by a single integration

$$\begin{aligned} \frac{dR^{(\eta)}}{dT} &= \frac{n_\chi}{2\pi} \int_{q_{\min}}^{q_{\max}} q dq \eta(\tilde{v}_{\min}) \left\{ (c_1 + d_1/q^2)^2 \mathcal{R}_{\text{SI}}(T, q) \right. \\ &\quad \left. + (\bar{c}_4 + \bar{d}_4/q^2)^2 \mathcal{R}_{\text{SD}}(T, q) \right\}, \end{aligned} \quad (11)$$

and is also implemented in the code.

Test examples of predicted differential count rates for a xenon detector with a kg-day exposure are summarized in Fig. 4. The agreement of dR/dT and $dR^{(\eta)}/dT$ is found to be excellent.

IV. COMPARISONS, DISCUSSIONS, AND NEW EXCLUSION LIMITS

The comparison of RRPA and RFCA photoionization cross sections with experiments for xenon in Fig. 1 has demonstrated the combined effect from exchange and correlation. (Taking into comparison the works of Refs. [53, 54], which had exchange effect included, one can judge that the correlation effect is more important.) Now we further examine their differences in the predictions of dR/dT in DM-xenon (DM-germanium) scattering in Fig. 5 for the test examples given above. In terms of percentage differences:

$$\left(\frac{dR/dT(\text{RRPA})}{dR/dT(\text{RFCA})} - 1 \right) \times 100\%$$

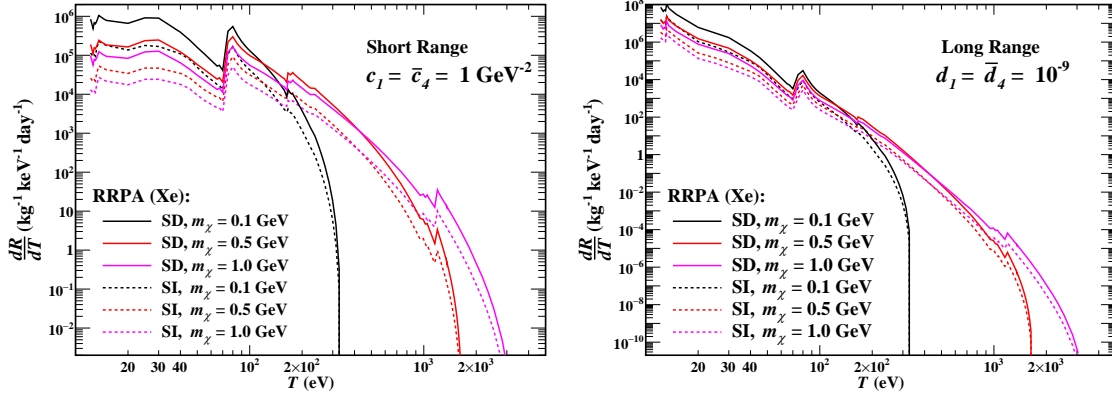


Figure 4. Differential count rates dR/dT due to the SI (dashed) or SD (solid) χ - e short-range (left) or long-range (right) interaction for a xenon detector with a kg-day exposure calculated by RRPAs response functions.

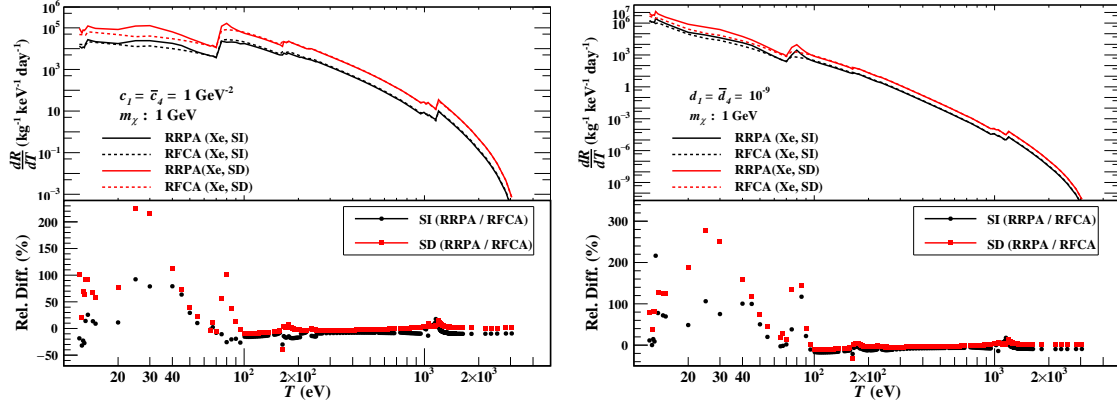


Figure 5. Comparison of the RRPAs with the RFCA predictions of $\frac{dR}{dT}$ for the $m_\chi = 1$ GeV case in Fig. 4. The bottom inset shows their percentage difference defined in the text. III B.

one can see that for $T \gtrsim 300$ eV, the agreement between RRPAs and RFCA is generally within 20%, except around the ionization thresholds ~ 1 keV.

However, for $T \lesssim 300$ eV, one clearly sees larger discrepancies. In this energy range, the electrons of xenon are ionized from three outermost shells $5p$, $5s$, and $4d$. From the previous discussion of how typical independent particle treatments failed to achieve reasonable agreement with photoabsorption data in the similar energy range, this is not unexpected. Furthermore, because the exchange and correlation effects are both range-dependent, their corrections to DM-impact ionization with the SR or LR DM-electron interaction would differ, which can be seen by comparing the left and right panels.

In the Figure 6, we compare our RRPAs with a few previous works including our previous

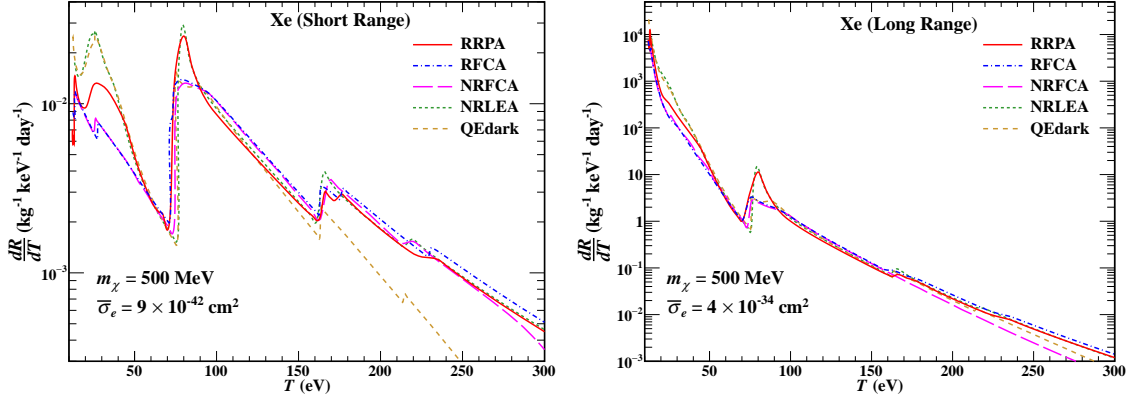


Figure 6. Comparison of the differential rate as a function of energy transfer for a Xe atom, calculated using several models: this work (RRPA, red), relativistic FCA (blue), non-relativistic FCA (magenta), NRLEA [28] (green), and the QEDark [6] (golden yellow). The calculations assume a dark matter mass $m_\chi = 500$ MeV and interaction strengths of (left) $c_1 = 5.28 \times 10^{-4}$ and (right) $d_1 = 4.89 \times 10^{-11}$ (equivalent to $\sigma_e = 9 \times 10^{-42} \text{ cm}^2$ and $\bar{\sigma}_e = 4 \times 10^{-34} \text{ cm}^2$, respectively, in Ref. [6]).

RFCA and nonrelativistic RFCA [10], and two other nonrelativistic calculations Ref. [28] (NRLEA, where LEA stands for local exchange approximation), and Ref. [6] (QEDark), reconstructed from the atomic ionization form factors provided in the codes AtMolDM [58] and QEdark [59] respectively.

Two important atomic ingredients: relativistic [10] and exchange [28] effects have been discussed previously. The former can be seen by the comparison of RFCA and NRFCA, as the difference is caused solely by solving the Dirac and Schrödinger equation, respectively, for the atomic wave functions. The latter can be seen by the comparison of NRFCA and the NRLEA. While both approaches are based on solving one-body Schrödinger equation for the final state, the difference is on the formulations of the averaged central field potential felt by the ionized electron. NRFCA only includes the direct (Hartree) term, but NRLEA further adds an approximate, local exchange potential. Even though the exchange potential is not formulated self-consistently, the difference between NRLEA and NRFCA should still give some measure of the exchange effect. Generally speaking, it enhances the event rate at low energies ($T \lesssim 50 \text{ eV}$), and suppresses at higher energies ($T > 100 \text{ eV}$).

With RRPA, we are able to incorporate the third important atomic ingredient: the correlation effect, along with the relativistic and exchange effects, in one self-consistent

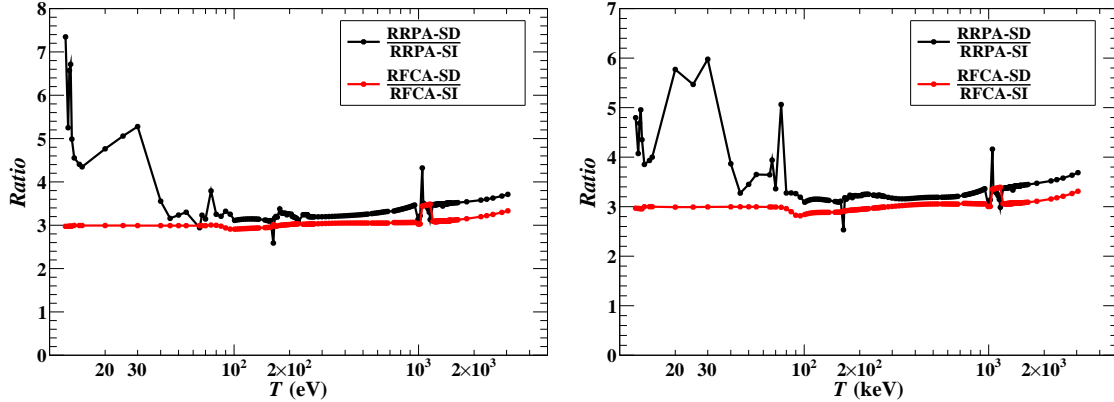


Figure 7. Ratios of the differential rates due to the SD versus SI DM-electron interactions of short- (left) and long- (right) range with $m_\chi = 1$ GeV.

framework. From the comparison of the RRPA and RFCA results, we see the combined exchange and correlation effect enhances the event rate at low energies in 20–50 eV and suppresses at higher energies. While not exactly the same as the previous NRLEA-NRFCA comparison (both have no correlation effect), the general trend is quite consistent.

At last, we should point out an interesting consequence of combining relativistic, exchange, and correlation effects in low-energy DM-electron scattering. It was pointed in Refs. [3, 15, 42], and explained in detail in Ref. [20], the leading-order SD and SI DM-electron interactions can not be distinguished in DM scattering off unpolarized targets, given that the atomic electrons behaves as a non-relativistic, independent particle assembly. In this case, the differential count rates of SI and SD scattering events only differ by a constant factor of 3, so are not linearly independent.

As shown in Fig. 7, the SD-SI ratio of dR/dT by RFCA has deviation from the factor of 3 but only in $T \gtrsim 1$ keV.⁵ It can be attributed to the fact that the spin-orbit interaction, as a part of the relativistic effect, is more pronounced for inner-shell electrons whose ionizations dominate at high energy transfer. With RRPA further including the exchange and correlation effects, we found the SD-SI ratio deviates from 3 substantially at low energies of $T \lesssim 100$ eV. This implies that the SD DM-electron interaction can possibly be differentiated from the SI one, and treated as an independent component of DM-electron interactions in conventional DM direct searches with unpolarized detector media.

While we will defer further theory explanations for future work, we can comment that

⁵ We note a coding mistake was identified in the work of Ref. [20] that underestimates the relativistic effect in the SD part. An erratum is in preparation.

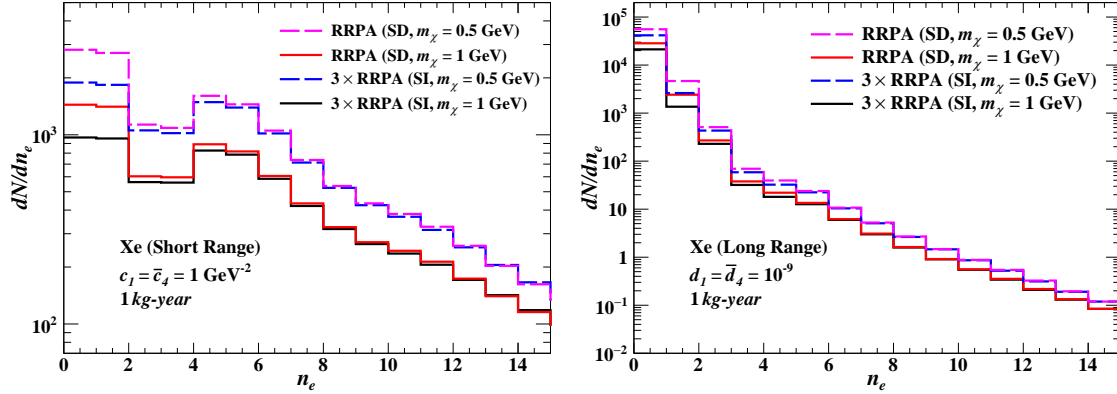


Figure 8. Comparisons of the expected event numbers due to the SD and SI DM-electron short- (left) and long-ranged (right) interactions as a function of the ionized electron number. The SI event numbers are multiplied by the scaling factor of 3, such that differences of the SD versus SI spectral shapes can be clearly seen.

such enhanced spin-dependent effect due to relativistic many-body physics at low T is not unexpected. For ground-state xenon, the spin-orbit splitting of the two most outer shells $E_{5p_{3/2}} - E_{5p_{1/2}} = 1.3 \text{ eV}$, which is not small: $\sim 10\%$ of the first ionization energy $-E_{5p_{3/2}} = 12.1 \text{ eV}$. For ground-state atomic germanium, while $E_{4p_{1/2}} - E_{4p_{3/2}} = 0.2 \text{ eV}$ seems smaller at $\sim 3\%$ of the first ionization energy $-E_{4p_{1/2}} = 7.8 \text{ eV}$, one should take note that the ordering of $4p_{1/2}$ and $4p_{3/2}$ orbitals is reversed, in contrary to the usual Landé interval rule.

In Fig. 8, we convert the differential rate (dR/dT) into the expected event numbers as a function of ionized electron number (dN/dn_e) through the following procedure. First, the recoil energy of the primary electron, denoted as E_r , is calculated by subtracting the average energy required to create one free quantum in liquid xenon (W) from the total energy transferred (T):

$$E_r = T - W. \quad (12)$$

Recent measurements indicate that the value for W is 11.5 eV [60, 61]. The maximum number of electrons (N_{max}) which include the primary and additional quanta from de-excitation, is obtained from the charge yield (Q_y) measured in [21] as

$$N_{max} = E_r \cdot Q_y. \quad (13)$$

The expected event rate is evaluated from the differential recoil spectrum dR/dE_r using the

following equation,

$$\frac{dN}{dn_e} = \int_{E_r^{min}}^{E_r^{max}} \frac{dR}{dE_r} \text{Binomial}(n_e; N_{max}; f_e) dE_r. \quad (14)$$

where n_e follows a binomial distribution with N_{max} trials and success probability of $f_e = 0.83$ [6]. Note that our approach of converting dR/dT to dN/dn_e differs slightly from Ref [6].

The expected event numbers as a function of ionized electron number n_e , assuming a xenon detector with 1 kg-year exposure and a 1-GeV DM particle is illustrated in Figure 8. One can easily observe their differences in spectral shapes in comparison to the corresponding SI ones multiplied by the factor of 3. This definitely will enrich the direct search data analyses focusing at low energies, for example, the recent XENON1T SE data set [21].

New exclusion limits

Dual-phase liquid xenon detectors have emerged as a vital technology in the search for dark matter, particularly for light dark matter (LDM), due to their exceptional sensitivity to ionization events down to the level of a single electron. This remarkable ability to detect single-electron ionization has greatly advanced the study of dark matter interactions, especially those involving electron scattering. Several key experiments using these detectors, such as XENON10, XENON100, XENON1T, PANDAX-II, and XENONnT, have made substantial contributions to the growing body of data in dark matter research.

Each of these experiments focuses on detecting dark matter by observing its possible interactions with atomic nuclei or electrons within the xenon target material. To explore and set exclusion limits on SI or SD DM-electron interactions and dark matter mass, data from experiments including XENON10 [62], XENON100 [63], XENON1T [13], and PANDAX-II [19] are analyzed in comparison with theoretical differential rate calculated by our RRPA response functions.

Under a conservative assumption that all observed events could be attributed to potential DM-electron scattering, upper limits at a 90% confidence level (C.L.) have been derived for both short- and long-range interactions, following the same methodology as outlined in previous studies, such as Refs. [10, 20]. These limits are shown in Fig. 9. The DM-free-electron scattering cross section is $\sigma_e = c_1^2 \mu_{\chi e}^2 / \pi$ or $\sigma_e = d_1^2 \mu_{\chi e}^2 / (\pi m_e^4 \alpha^4)$ for the SI SR or LR interaction, respectively. For the SD interaction, the coupling constant squared is

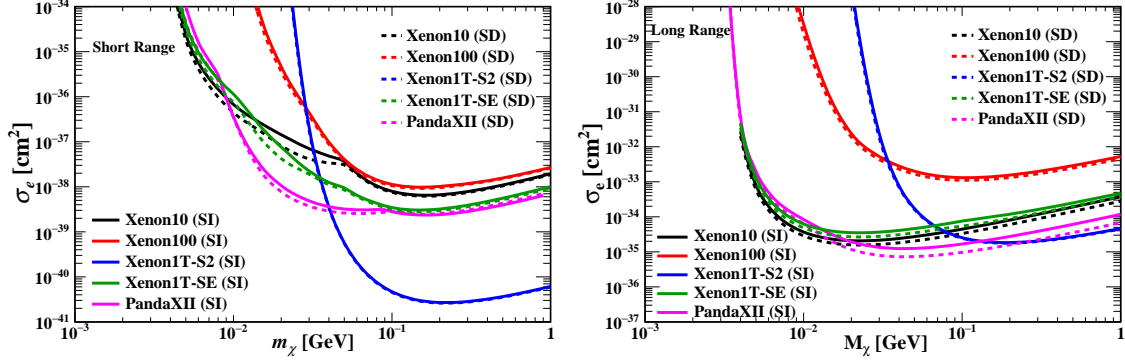


Figure 9. The exclusion limits at 90% confidence level (C.L.) on spin-independent and spin-dependent short-range (left panel) and long-range (right panel) DM-electron interactions, as functions of dark matter mass, are derived from XENON experiment data, including XENON10 (black) [4], XENON100 (red) [6], XENON1T-S2 (blue) [13], XENON1T-S2 (green) [21], and PandaX-II [19].

changed to $3\bar{c}_4^2$ or $3\bar{d}_4^2$, accordingly. In the case of XENON1T, the data from both the XENON1T S2-only and the XENON1T single-electron (SE) data set have been analyzed. The XENON1T-SE [13] data set has a lower threshold, which allows it to probe lower dark matter masses, but near the threshold the background levels becomes higher. As a result, while the XENON1T-SE [21] data can explore lower mass ranges, the constraints degrade at higher masses due to the increased background noise.

For both the SR and LR SI interactions, the limits set by the XENON1T-S2 data, which has a relatively high-threshold at 186 eV, become slightly less stringent from RFCA to RRPA. This can be seen in Fig. 5 that RFCA predicts a slightly bigger count rate for most region in $T \gtrsim 186$ eV. On the other hand, with the low-threshold XENON10 data, at $1 n_e$ (XENON1T-SE and PandaXII alike), the situation is more subtle. As Fig. 5 shows, the energy region that RRPA differs from RFCA is $T \lesssim 300$ eV, and predicts a bigger count rate in $T \lesssim 50$ eV. As a result, the exclusion limits on the LR SI interaction or the SR interaction with a low-mass DM particle are improved from RFCA to RRPA, since in both cases the scattering events are dominated by low energy bins.

While similar reasoning applies the the case of the SD interactions, one should first note that the scaling factor of 3 is also built-in in the DM scattering with a free electron, i.e. $\sigma_e^{(SD)} = 3\sigma_e^{(SI)}$, given the same coupling constants $c_1 = \bar{c}_4$ for the SR, or $d_1 = \bar{d}_4$ for the LR interaction. If the unpolarized atomic response functions follow the same scaling, the

exclusion limit on $\sigma_e^{(\text{SD})}$ would be exactly the same as the one on $\sigma_e^{(\text{SI})}$. This is what can be seen in Fig. 9: The XENON1T-S2 exclusion curves for the SD (in dashed blue) interactions can barely be distinguished from the ones for the SI counterparts (in solid blue). As one sees in Fig. 7, the deviation from the scaling factor is modest in $T \gtrsim 186$ eV, and is only sizable in the energy range where the count rate is small. However, for data sets with low energy thresholds, the substantial scaling deviation ($T \lesssim 300$ eV in Fig. 7) result in not only a energy spectral shape different from the SI case, but also excess counts (see Fig. 8) that give rise to the more stringent exclusion limits than the SI interactions.

V. SUMMARY

In this work, we applied a state-of-the-arts atomic technique, the (multiconfiguration) relativistic random phase approximation, to compute the response functions of sub-GeV light dark matter particles scattered off the xenon and germanium atoms through either spin-independent or spin-dependent dark matter-electron interactions at leading order in effective field theory expansion. Our method, unlike most existing atomic approaches applied to sub-GeV dark matter searches, is successfully benchmarked by photoabsorption data in the energy range of tens of eV to 30 keV, which covers the kinetic energy range of dark matter particles with masses in between MeV and GeV. In addition to previously-identified contributions from relativistic and exchange effects, the correlation effect not included in independent particle frameworks is incorporated by RPA. Surprisingly, these effects combined to cause different energy dependence of the spin-dependent versus the spin-independent responses, such that two interactions can be distinguished at low energies, unlike previous results and argument based on the independent particle picture. Lastly, we use these high-quality response functions to place reliable exclusion limits with data from current experiments including XENON10, XENON100, XENON1T, PANDAX-II, and XENONnT.

The response functions computed in this work are available for download. The codes that automatize the process of getting detector count rate predictions are also provided. Our future plan includes extending the parameter space of response functions, decomposing the response functions by individual atomic shells, and including other atomic species that serve as detector materials.

ACKNOWLEDGMENTS

This work was supported in part under Contract Nos. 111-2112-M259-007 (C.-P. L.), 111-2811-M-259-014 (M. K. P.), from the Ministry of Science and Technology; 112-2112-M259-014 (C.-P. L.), 112-2811-M-259-006 (C.-P. W.), 112-2112-M-002-027 and 113-2112-M-002-012 (J.-W. C.), 113-2112-M-001-053-MY3 (H. T. W.) from the National Science and Technology Council; and 2021-2024/TG2.1 from the National Center for Theoretical Sciences of Taiwan; the Canada First Research Excellence Fund through the Arthur B. McDonald Canadian Astroparticle Physics Research Institute (C.-P. W.); and Contract F.30-584/2021 (BSR), UGC-BSR Research Start Up Grant, India; the PURSE grant and FIST program of Department of Science & Technology, India (L. S.). We thank the Academia Sinica Grid-computing Centre for providing the computing facility that makes this work possible, and its staff for excellent technical supports. JWC thanks the InQubator for Quantum Simulation in Seattle and the Yukawa Institute for Theoretical Physics at Kyoto Univ. for hospitality.

Appendix: Brief Overview of (MC)RRPA Theory

While there are many ways to formulate the (MC)RRPA theory, in this appendix we follow the route of time-dependent Dirac-Hartree-Fock theory (the relativistic version of time-dependent Hartree-Fock), as it becomes particularly handy when it comes the computation of the many-body wave functions and transition amplitudes.

General Formalism

Consider a time-dependent Hamiltonian of an atomic system with N electrons given by:

$$H(t) = H_0 + V(t). \quad (\text{A.1})$$

The time-independent Hamiltonian

$$H_0 = \sum_{i=1}^N h_i + \sum_{i<j}^N \frac{e^2}{r_{ij}}, \quad (\text{A.2})$$

$$h_i = \vec{\alpha}_i \cdot \vec{p}_i + \beta m_e - \frac{Z}{r_i}, \quad (\text{A.3})$$

governs the usual atomic structure with the Dirac Hamiltonian, nuclear Coulomb attraction, and electron-electron repulsion. The time-dependent interaction that causes atomic transitions is assumed to take a one-body harmonic form

$$V(t) = \sum_{i=1}^N v_i e^{-i\omega t} + \sum_{i=1}^N v_i^\dagger e^{+i\omega t} \equiv V_+ e^{-i\omega t} + V_- e^{i\omega t}, \quad (\text{A.4})$$

It will be treated perturbatively in the end, and become clear that the $v_i(v_i^\dagger)$ term results in a single electron (de-)excitation of energy ω . In this work, $V(t)$ is the DM-electron interaction due to Eq. (1).

To solve the many-body wave function $|\Psi(t)\rangle$, the equation of motion

$$i \frac{\partial}{\partial t} |\Psi(t)\rangle = H(t) |\Psi(t)\rangle, \quad (\text{A.5})$$

can be recast into a Frenkel variational form:

$$\left\langle \delta\Psi(t) \left| \left[i \frac{\partial}{\partial t} - H(t) \right] \right| \Psi(t) \right\rangle = 0. \quad (\text{A.6})$$

By further factoring out the time evolution due to the unperturbed eigenenergy, E , i.e.,

$$|\Psi(t)\rangle = e^{-iEt} |\Psi'(t)\rangle, \quad (\text{A.7})$$

the variational solution of $|\Psi'(t)\rangle$ is

$$\left\langle \delta\Psi'(t) \left| \left[E + i \frac{\partial}{\partial t} - H(t) \right] \right| \Psi'(t) \right\rangle = 0. \quad (\text{A.8})$$

In the spirit of Hartree-Fock (HF) theory, we seek an approximate solution to Eq. (A.8) based on Slater determinants with relativistic Hamiltonian, referred as Dirac-Fock (DF) theory henceforth. First, $|\Psi'(t)\rangle$ is formed by a linear combination of configuration state functions (CSFs) $|\Phi_A(t)\rangle$

$$|\Psi'(t)\rangle = \sum_A C_A(t) |\Phi_A(t)\rangle, \quad (\text{A.9})$$

where A is the configuration index, $C_A(t)$ the time-dependent weight. Note that the multi-configuration (MC) feature is simply reflected by the number of possible A 's is more than one. A configuration A for a N -electron state is specified by the N electron orbitals being occupied and labeled by $\{\alpha_1, \alpha_2, \dots, \alpha_N\}$ with each α collectively denotes four quantum numbers: principle n_α (or reduced wave number k_α for a continuum state), orbital and total

angular momentum l_α and j_α (in relativistic cases, they are usually combined as κ_α , which is $\mp(j_\alpha + 1/2)$ for $l_\alpha = j_\alpha \pm 1/2$), and the z -axis projection of total angular momentum m_α . The CSFs are taken to be the Slater determinant of all occupied time-dependent single electron orbitals, denoted by

$$|u_\alpha(t)\rangle = |n_\alpha l_\alpha j_\alpha m_\alpha; t\rangle \equiv |am_\alpha; t\rangle. \quad (\text{A.10})$$

The equation of motions for $C_A(t)$'s and $u_\alpha(t)$'s are derived by varying $C_A^*(t)$'s and $u_\alpha^\dagger(t)$ in Eq. (A.8) with the constraints of probability conservation

$$\langle \Psi'(t) | \Psi'(t) \rangle = 1. \quad (\text{A.11})$$

This can be furnished by the following conditions

$$\sum_A C_A^*(t) C_A(t) = 1, \quad (\text{A.12})$$

$$\langle u_\alpha(t) | u_\beta(t) \rangle = \delta_{\alpha\beta}, \quad (\text{A.13})$$

where orbital wave functions are required to be orthonormal at all times, and configuration weights satisfy the normalization condition. This leads to

$$(E + i\frac{\partial}{\partial t})C_A(t) + \sum_B \left\langle \Phi_A(t) \left| i\frac{\partial}{\partial t} - H(t) \right| \Phi_B(t) \right\rangle = 0, \quad (\text{A.14})$$

$$\sum_{AB} C_A^*(t) C_B(t) \frac{\partial}{\partial u_\alpha^\dagger(t)} \left\langle \Phi_A(t) \left| i\frac{\partial}{\partial t} - H(t) \right| \Phi_B(t) \right\rangle = \sum_\beta \gamma_{\alpha\beta}(t) u_\beta(t), \quad (\text{A.15})$$

where $\partial/\partial u_\alpha^\dagger(t)$ should be understood as a functional derivative acting on the many-body matrix element that follows, and $\gamma_{\alpha\beta}(t)$ the Lagrange multiplier that enforces the orthonormality of single-particle orbitals.

As the time-dependent interaction $V(t)$ is harmonic in time, the solutions of $C_A(t)$, $u_\alpha(t)$, and $\gamma_{\alpha\beta}(t)$ can assume the following harmonic expansions with time dependence explicitly factored out by $e^{\pm i\omega t}$:

$$C_A(t) = C_A + [C_A]_+ e^{-i\omega t} + [C_A]_- e^{+i\omega t} + \dots, \quad (\text{A.16})$$

$$u_\alpha(t) = u_\alpha + w_{\alpha+} e^{-i\omega t} + w_{\alpha-} e^{+i\omega t} + \dots, \quad (\text{A.17})$$

$$\gamma_{\alpha\beta}(t) = \gamma_{\alpha\beta} + [\gamma_{\alpha\beta}]_+ e^{-i\omega t} + [\gamma_{\alpha\beta}]_- e^{+i\omega t} + \dots, \quad (\text{A.18})$$

where “...” denotes higher harmonic terms. The so-called random phase approximation (RPA) refers to truncation of the series to the first harmonic terms with all “...” terms omitted. Viewing $V(t)$ as a perturbation, RPA corresponds to a time-dependent perturbation theory to first order, so sometimes is also called the linear response theory. The time-independent configuration weights, C_A and $[C_A]_{\pm}$, and orbital wave functions u_{α} and $w_{\alpha\pm}$ are now subject to the following constraints

$$\sum_A C_A^* C_A = 1 \quad (\text{A.19})$$

$$\sum_A [C_A]_{\mp}^* C_A + C_A^* [C_A]_{\pm} = 0, \quad (\text{A.20})$$

$$\langle u_{\alpha} | u_{\beta} \rangle = \delta_{\alpha\beta}, \quad (\text{A.21})$$

$$\langle w_{\alpha\mp} | u_{\beta} \rangle + \langle u_{\alpha} | w_{\alpha\pm} \rangle = 0. \quad (\text{A.22})$$

Because the perturbation is a one-body operator, one thing it can do is promoting an electron in a filled orbital, u_{α} , to an unoccupied state (in our case in continuum). As the energy increases (manifested by $e^{-i\omega t}$), this state is labeled by $w_{\alpha+}$ and can be expanded by unoccupied orbitals. A calculation that only takes into these states is called Tamm-Dancoff approximation (TDA). The improvement of RPA over TDA is introducing the correlation effect to the ground state wave function, such that it contains other CSFs than the ones in the MCDF reference state. As a result, the other thing that the one-body operator can do is demoting an electron from a filled orbital of higher energies back to a vacancy in u_{α} . As the energy decreases (manifested by $e^{+i\omega t}$), this state is labeled by $w_{\alpha-}$. Therefore, RPA incorporates the correlation effects in the ground and excited states with equal footing.

Using the harmonic expansion above, at zeroth order, one obtains the MCDF equations for unperturbed weights C_A and orbitals u_{α} :

$$EC_A - \sum_B \langle \Phi_A | H_0 | \Phi_B \rangle C_B = 0, \quad (\text{A.23})$$

$$\sum_{AB} C_A^* C_B \frac{\partial}{\partial u_{\alpha}^{\dagger}} \langle \Phi_A | H_0 | \Phi_B \rangle = \sum_{\beta} \gamma_{\alpha\beta} u_{\beta}. \quad (\text{A.24})$$

At first order, one obtains the MCRRPA equations for $[C_A]_{\pm}$ and $w_{\alpha\pm}$:

$$\begin{aligned}
& (E \pm \omega) [C_A]_{\pm} - \sum_B (\langle \Phi_A | H_0 | \Phi_B \rangle [C_B]_{\pm} + \langle \Phi_A | H_0 | \Phi_B \rangle_{\pm} C_B) \\
& = \sum_B \langle \Phi_A | V_{\pm} | \Phi_B \rangle C_B, \tag{A.25}
\end{aligned}$$

$$\begin{aligned}
& \sum_{AB} C_A^* C_B \frac{\partial}{\partial u_{\alpha}^{\dagger}} \left\langle \Phi_A \left| i \frac{\partial}{\partial t} - H_0 \right| \Phi_B \right\rangle_{\pm} - \sum_{AB} ([C_A]_{\mp}^* C_B + C_A^* [C_B]_{\pm}) \frac{\partial}{\partial u_{\alpha}^{\dagger}} \langle \Phi_A | H_0 | \Phi_B \rangle \\
& - \sum_{\beta} \gamma_{\alpha\beta} w_{\beta\pm} + [\gamma_{\alpha\beta}]_{\pm} u_{\beta} = \sum_{AB} C_A^* C_B \frac{\partial}{\partial u_{\alpha}^{\dagger}} \langle \Phi_A | V_{\pm} | \Phi_B \rangle. \tag{A.26}
\end{aligned}$$

Note that the energy functional $\langle \Phi_A | i \frac{\partial}{\partial t} - H_0 | \Phi_B \rangle_{\pm}$ contains the perturbed wave function $w_{\alpha\pm}$ in the ket state $|\Psi_B\rangle$ or $w_{\alpha\mp}^{\dagger}$ in the bra state $\langle \Psi_A|$.

Applications to Ionization Processes of Xenon and Germanium

Up to this stage, the MCDF and MCRRPA equations are completely general, and can involve an arbitrary number of CSFs. To bring the numerical computations to a manageable scale, one has to limit the numbers of CSFs and the single electron orbitals on which they are built. As we deal in this work the problem of atomic ionization by one-body perturbations caused by DM-electron interactions, the most relevant CSFs are the ones that describe the atomic ground state, and the one-particle-one-hole excitations from the ground state that describe the ion-plus-one-free-electron final states.

For xenon, a closed-shell atom, we follow the conventional HF approach and treat its ground state wave function at zeroth order, the reference state, as a single Slater determinant with the configuration $[\text{Kr}]4d^{10}5s^25p^6$, and this gives the set of the unperturbed orbitals u_{α} 's. As all orbitals are completely filled, its total angular momentum and parity is 0^+ . For germanium, a divalent atom, its ground state configuration at zeroth order is $[\text{Ar}]3d^{10}4s^24p^2$ with total angular momentum and parity being 0^+ . In this case, the reference state contains two CSFs: one with $4p_{3/2}^2$, the other with $4p_{1/2}^2$. Both can form a 0^+ state, but are made of different $4p$ orbitals. For this distinction, the computations of xenon and germanium are labeled as RRPA and MCRRPA, respectively.

With these considerations, the above MCDF and MCRRPA equations can be made more explicitly. Here we use the case of xenon as an example. Because the reference state has

only one configuration, there is no equation for C_A 's to be solved (only $C_1 = 1$). The orbital equation at zeroth order becomes:

$$\left[h + v_{12}^{(\text{DF})} \right] u_\alpha(\vec{r}) = \epsilon_\alpha u_\alpha(\vec{r}) + \sum_{\beta \neq \alpha} \gamma_{\alpha\beta} u_\beta(\vec{r}), \quad (\text{A.27})$$

with

$$v_{12}^{(\text{DF})} u_\alpha(\vec{r}) = \sum_{\beta} \int d^3 r' \frac{e^2}{|\vec{r} - \vec{r}'|} \left[u_\beta^\dagger(\vec{r}', t) u_\beta(\vec{r}', t) u_\alpha(\vec{r}, t) - u_\beta^\dagger(\vec{r}', t) u_\beta(\vec{r}, t) u_\alpha(\vec{r}', t) \right]. \quad (\text{A.28})$$

The Dirac-Fock (DF) potential is simply a relativistic version of the conventional HF potential which consists of the direct and exchange terms, and the diagonal Lagrange multiplier $\gamma_{\alpha\alpha}$ is identified as the orbital energy ϵ_α . The orbital equation at first order becomes

$$\left[h + v_{12}^{(\text{RPA})} \right] w_{\alpha\pm}(\vec{r}) = (\epsilon_\alpha \pm \omega) w_{\alpha\pm}(\vec{r}) + v_\pm u_\alpha(\vec{r}) + \sum_{\beta} [\gamma_{\alpha\beta}]_{\pm} u_\beta(\vec{r}) + \sum_{\beta \neq \alpha} \gamma_{\alpha\beta} w_{\beta\pm}(\vec{r}), \quad (\text{A.29})$$

with

$$v_{12}^{(\text{RPA})} w_{\alpha\pm}(\vec{r}) = v_{12}^{(\text{DF})} w_{\alpha\pm}(\vec{r}) + \sum_{\beta} \int d^3 r' \frac{e^2}{|\vec{r} - \vec{r}'|} \left[u_\beta^\dagger(\vec{r}') w_{\beta\pm}(\vec{r}') u_\alpha(\vec{r}) - u_\beta^\dagger(\vec{r}') w_{\beta\pm}(\vec{r}) u_\alpha(\vec{r}') w_{\beta\mp}^\dagger(\vec{r}') u_\beta(\vec{r}') u_\alpha(\vec{r}) - w_{\beta\mp}^\dagger(\vec{r}') u_\beta(\vec{r}') u_\alpha(\vec{r}') \right]. \quad (\text{A.30})$$

Moving on to open-shell atoms, the algebra becomes more cumbersome as the numbers of valence electrons increase. For divalent systems of zero total angular momenta, the details can be found in Ref. [32].

After the zeroth-order ground state configurations are fixed, the excited state configurations are determined by the transition operators prescribed by the perturbation. As rotation and parity are good symmetries of H_0 , a spherical multipole decomposition of the perturbing field is an efficient way to reduce the number of CSFs to be included. Consider a spherical multipole operator of angular momentum J and parity $(-1)^\Pi$ ($\Pi = 0$ for even and $\Pi = 1$ for odd), because both xenon and germanium initially (I) are at $(J_I, \Pi_I) = (0, 0)$ states, their final (F) states will have the same quantum numbers as the transition operator, i.e., $(J_F, \Pi_F) = (J, \Pi)$. Furthermore, because the transition operator is one-body, the one-particle-one-hole states it creates ($w_{\alpha+} - u_\alpha$) or annihilate ($u_\alpha - w_{\alpha-}$) must couple to the desired state of (J, Π) .

Let us use the \hat{C}_1 transition operator $(J, \Pi) = (1, 1)$, which is part of spin-independent DM-electron scattering, as an example. First, we note that by Wigner-Eckart theorem, all

the algebra related to magnetic quantum numbers can be carried out straightforwardly, so we abbreviate a quantum label α to its reduced version a . When a $a = 5p_{1/2}$ electron is ionized to continuum by \hat{C}_1 , the possible final partial waves can only be $\epsilon s_{1/2}$ and $\epsilon d_{3/2}$, with ϵ fixed by energy conservation. As a result, the quantum label of $a+$ can be either $\epsilon s_{1/2}$ and $\epsilon d_{3/2}$. On the other hand, for $a = 5p_{3/2}$, $a+$ can be $\epsilon s_{1/2}$, $\epsilon d_{3/2}$, or $\epsilon d_{5/2}$. For other 15 core orbitals of different a 's, there are 37 more distinct $a+$ orbitals which can be mixed. The enumeration for $a-$ states follows the same angular momentum and parity selection rules, except the energy eigenvalues are different. Altogether, at zeroth order, the DF orbital equation is a set of 17 coupled integral-differential equations of $u_a(\vec{r})$'s. With the input from zeroth-order results, the RRPA orbital equation is a set of 84 coupled integral-differential equations of $w_{a\pm}(\vec{r})$'s and solved by self-consistent field methods. This is clearly more numerically-intensive task than the decoupled equations one normally encounter in Hartree frozen core, or local exchange approximation. On the other hand, as the equation shows, it is a method that goes beyond the typical mean-field approaches that consider the correlation effects in both the ground and excited states.

Finally, the transition matrix element of a spherical multipole operator \hat{O}_J^M is simply calculated by the unperturbed and perturbed orbitals, u_α and $w_{\alpha\pm}$, that make up the initial and final states, i.e.,

$$\langle \Psi_f | \hat{O}_J^M | \Psi_i \rangle = \sum_{\alpha} \Lambda_{\alpha} (\langle w_{\alpha+} | \hat{O}_J^M | u_{\alpha} \rangle + \langle u_{\alpha} | \hat{O}_J^M | w_{\alpha-} \rangle), \quad (\text{A.31})$$

where α run through all the occupied orbitals in the reference state. For a core orbital, the weighting factor Λ_{α} is always 1, and this applies to all xenon orbitals and germanium orbitals other than $4p$. As we choose the germanium divalent configuration to be $C_1 |4p_{1/2}^2\rangle + C_2 |4p_{3/2}^2\rangle$, the weighting factors for $4p_{1/2}$ and $4p_{3/2}$ are $|C_1|^2$ and $|C_2|^2/2$, respectively, where the extra 1/2 factor is due to the shell being only half-filled.

[1] M. Battaglieri *et al.*, US Cosmic Visions: New Ideas in Dark Matter 2017: Community Report, in *U.S. Cosmic Visions: New Ideas in Dark Matter College Park, MD, USA, March 23-25, 2017* (2017) arXiv:1707.04591 [hep-ph].

- [2] R. Essig *et al.*, Snowmass2021 Cosmic Frontier: The landscape of low-threshold dark matter direct detection in the next decade, in *Snowmass 2021* (2022) arXiv:2203.08297 [hep-ph].
- [3] J. Kopp, V. Niro, T. Schwetz, and J. Zupan, DAMA/LIBRA and leptonically interacting Dark Matter, *Phys. Rev. D* **80**, 083502 (2009), arXiv:0907.3159 [hep-ph].
- [4] R. Essig, A. Manalaysay, J. Mardon, P. Sorensen, and T. Volansky, First Direct Detection Limits on sub-GeV Dark Matter from XENON10, *Phys. Rev. Lett.* **109**, 021301 (2012), arXiv:1206.2644 [astro-ph.CO].
- [5] B. M. Roberts, V. A. Dzuba, V. V. Flambaum, M. Pospelov, and Y. V. Stadnik, Dark matter scattering on electrons: Accurate calculations of atomic excitations and implications for the DAMA signal, *Phys. Rev. D* **93**, 115037 (2016), arXiv:1604.04559 [hep-ph].
- [6] R. Essig, T. Volansky, and T.-T. Yu, New Constraints and Prospects for sub-GeV Dark Matter Scattering off Electrons in Xenon, *Phys. Rev. D* **96**, 043017 (2017), arXiv:1703.00910 [hep-ph].
- [7] P. Agnes *et al.* (DarkSide), Constraints on Sub-GeV Dark Matter-Electron Scattering from the DarkSide-50 Experiment, *Phys. Rev. Lett.* **121**, 111303 (2018), arXiv:1802.06998 [astro-ph.CO].
- [8] M. Crisler, R. Essig, J. Estrada, G. Fernandez, J. Tiffenberg, M. Sofo haro, T. Volansky, and T.-T. Yu (SENSEI), SENSEI: First Direct-Detection Constraints on sub-GeV Dark Matter from a Surface Run, *Phys. Rev. Lett.* **121**, 061803 (2018), arXiv:1804.00088 [hep-ex].
- [9] R. Agnese *et al.* (SuperCDMS), First Dark Matter Constraints from a SuperCDMS Single-Charge Sensitive Detector, *Phys. Rev. Lett.* **121**, 051301 (2018), [Erratum: *Phys.Rev.Lett.* **122**, 069901 (2019)], arXiv:1804.10697 [hep-ex].
- [10] M. K. Pandey, L. Singh, C.-P. Wu, J.-W. Chen, H.-C. Chi, C.-C. Hsieh, C.-P. Liu, and H. T. Wong, Constraints from a many-body method on spin-independent dark matter scattering off electrons using data from germanium and xenon detectors, *Phys. Rev. D* **102**, 123025 (2020), arXiv:1812.11759 [hep-ph].
- [11] O. Abramoff *et al.* (SENSEI), SENSEI: Direct-Detection Constraints on Sub-GeV Dark Matter from a Shallow Underground Run Using a Prototype Skipper-CCD, *Phys. Rev. Lett.* **122**, 161801 (2019), arXiv:1901.10478 [hep-ex].
- [12] B. Roberts and V. Flambaum, Electron-interacting dark matter: Implications from DAMA/LIBRA-phase2 and prospects for liquid xenon detectors and NaI detectors, *Phys. Rev. D* **100**, 063017 (2019), arXiv:1904.07127 [hep-ph].

- [13] E. Aprile *et al.* (XENON), Light Dark Matter Search with Ionization Signals in XENON1T, Phys. Rev. Lett. **123**, 251801 (2019), arXiv:1907.11485 [hep-ex].
- [14] A. Aguilar-Arevalo *et al.* (DAMIC), Constraints on Light Dark Matter Particles Interacting with Electrons from DAMIC at SNOLAB, Phys. Rev. Lett. **123**, 181802 (2019), arXiv:1907.12628 [astro-ph.CO].
- [15] R. Catena, T. Emken, N. A. Spaldin, and W. Tarantino, Atomic responses to general dark matter-electron interactions, Phys. Rev. Res. **2**, 033195 (2020), arXiv:1912.08204 [hep-ph].
- [16] Q. Arnaud *et al.* (EDELWEISS), First germanium-based constraints on sub-MeV Dark Matter with the EDELWEISS experiment, Phys. Rev. Lett. **125**, 141301 (2020), arXiv:2003.01046 [astro-ph.GA].
- [17] L. Barak *et al.* (SENSEI), SENSEI: Direct-Detection Results on sub-GeV Dark Matter from a New Skipper-CCD, Phys. Rev. Lett. **125**, 171802 (2020), arXiv:2004.11378 [astro-ph.CO].
- [18] D. W. Amaral *et al.* (SuperCDMS), Constraints on low-mass, relic dark matter candidates from a surface-operated SuperCDMS single-charge sensitive detector, Phys. Rev. D **102**, 091101 (2020), arXiv:2005.14067 [hep-ex].
- [19] C. Cheng *et al.* (PandaX-II), Search for Light Dark Matter-Electron Scatterings in the PandaX-II Experiment, Phys. Rev. Lett. **126**, 211803 (2021), arXiv:2101.07479 [hep-ex].
- [20] C.-P. Liu, C.-P. Wu, J.-W. Chen, H.-C. Chi, M. K. Pandey, L. Singh, and H. T. Wong, Spin-dependent dark matter-electron interactions, Phys. Rev. D **106**, 063003 (2022), arXiv:2106.16214 [hep-ph].
- [21] E. Aprile *et al.* (XENON), Emission of single and few electrons in XENON1T and limits on light dark matter, Phys. Rev. D **106**, 022001 (2022), arXiv:2112.12116 [hep-ex].
- [22] Z. Y. Zhang *et al.* (CDEX), Constraints on Sub-GeV Dark Matter–Electron Scattering from the CDEX-10 Experiment, Phys. Rev. Lett. **129**, 221301 (2022), arXiv:2206.04128 [hep-ex].
- [23] I. Arnquist *et al.* (DAMIC-M), First Constraints from DAMIC-M on Sub-GeV Dark-Matter Particles Interacting with Electrons, Phys. Rev. Lett. **130**, 171003 (2023), arXiv:2302.02372 [hep-ex].
- [24] P. Adari *et al.* (SENSEI), SENSEI: First Direct-Detection Results on sub-GeV Dark Matter from SENSEI at SNOLAB, (2023), arXiv:2312.13342 [astro-ph.CO].
- [25] J.-H. Liang, Y. Liao, X.-D. Ma, and H.-L. Wang, Revisiting general dark matter-bound-electron interactions, Phys. Rev. D **110**, L091701 (2024), arXiv:2405.04855 [hep-ph].

- [26] J.-H. Liang, Y. Liao, X.-D. Ma, and H.-L. Wang, A systematic investigation on dark matter-electron scattering in effective field theories, *JHEP* **07**, 279, arXiv:2406.10912 [hep-ph].
- [27] R. Essig, J. Mardon, and T. Volansky, Direct Detection of Sub-GeV Dark Matter, *Phys. Rev. D* **85**, 076007 (2012), arXiv:1108.5383 [hep-ph].
- [28] L. Hamaide and C. McCabe, Fueling the search for light dark matter-electron scattering with spherical proportional counters, *Phys. Rev. D* **107**, 063002 (2023), arXiv:2110.02985 [hep-ph].
- [29] A. R. Caddell, V. V. Flambaum, and B. M. Roberts, Accurate electron-recoil ionization factors for dark matter direct detection in xenon, krypton, and argon, *Phys. Rev. D* **108**, 083030 (2023), arXiv:2305.05125 [hep-ph].
- [30] S.-F. Ge, J. Sheng, and C.-Y. Xing, Relativistic Atomic Effects of Dark Matter Electron Scattering, arXiv:2509.14534 [hep-ph].
- [31] W. R. Johnson and C. D. Lin, Multichannel relativistic random-phase approximation for the photoionization of atoms, *Phys. Rev. A* **20**, 964 (1979).
- [32] K.-N. Huang and W. R. Johnson, Multiconfiguration relativistic random-phase approximation. Theory, *Phys. Rev. A* **25**, 634 (1982).
- [33] B. M. Roberts, V. V. Flambaum, and G. F. Gribakin, Ionization of atoms by slow heavy particles, including dark matter, *Phys. Rev. Lett.* **116**, 023201 (2016), arXiv:1509.09044 [physics.atom-ph].
- [34] R. Essig, M. Fernandez-Serra, J. Mardon, A. Soto, T. Volansky, and T.-T. Yu, Direct Detection of sub-GeV Dark Matter with Semiconductor Targets, *JHEP* **05**, 046, arXiv:1509.01598 [hep-ph].
- [35] S. Knapen, J. Kozaczuk, and T. Lin, PYTHON package for dark matter scattering in dielectric targets, *Phys. Rev. D* **105**, 015014 (2022), arXiv:2104.12786 [hep-ph].
- [36] S. M. Griffin, K. Inzani, T. Trickle, Z. Zhang, and K. M. Zurek, Extended calculation of dark matter-electron scattering in crystal targets, *Phys. Rev. D* **104**, 095015 (2021), arXiv:2105.05253 [hep-ph].
- [37] J. Fan, M. Reece, and L.-T. Wang, Non-relativistic effective theory of dark matter direct detection, *JCAP* **1011**, 042, arXiv:1008.1591 [hep-ph].
- [38] A. L. Fitzpatrick, W. Haxton, E. Katz, N. Lubbers, and Y. Xu, The Effective Field Theory of Dark Matter Direct Detection, *JCAP* **1302**, 004, arXiv:1203.3542 [hep-ph].
- [39] M. Cirelli, E. Del Nobile, and P. Panci, Tools for model-independent bounds in direct dark

- matter searches, *JCAP* **10**, 019, arXiv:1307.5955 [hep-ph].
- [40] N. Anand, A. L. Fitzpatrick, and W. C. Haxton, Weakly interacting massive particle-nucleus elastic scattering response, *Phys. Rev. C* **89**, 065501 (2014), arXiv:1308.6288 [hep-ph].
- [41] N. Anand, A. L. Fitzpatrick, and W. C. Haxton, Model-independent Analyses of Dark-Matter Particle Interactions, *Phys. Procedia* **61**, 97 (2015), arXiv:1405.6690 [nucl-th].
- [42] J.-W. Chen, H.-C. Chi, C. P. Liu, C.-L. Wu, and C.-P. Wu, Electronic and nuclear contributions in sub-GeV dark matter scattering: A case study with hydrogen, *Phys. Rev. D* **92**, 096013 (2015), arXiv:1508.03508 [hep-ph].
- [43] E. Del Nobile, Complete Lorentz-to-Galileo dictionary for direct dark matter detection, *Phys. Rev. D* **98**, 123003 (2018), arXiv:1806.01291 [hep-ph].
- [44] R. Catena, K. Fridell, and M. B. Krauss, Non-relativistic Effective Interactions of Spin 1 Dark Matter, *JHEP* **08**, 030, arXiv:1907.02910 [hep-ph].
- [45] T. Trickle, Z. Zhang, and K. M. Zurek, Effective field theory of dark matter direct detection with collective excitations, *Phys. Rev. D* **105**, 015001 (2022), arXiv:2009.13534 [hep-ph].
- [46] T. W. Donnelly and W. C. Haxton, Multipole operators in semileptonic weak and electromagnetic interactions with nuclei, *Atom. Data Nucl. Data Tabl.* **23**, 103 (1979).
- [47] B. Henke, E. Gullikson, and J. Davis, X-ray interactions: Photoabsorption, scattering, transmission, and reflection at $e = 50\text{-}30,000$ ev, $z = 1\text{-}92$, *Atomic Data and Nuclear Data Tables* **54**, 181 (1993).
- [48] J. Samson and W. Stolte, Precision measurements of the total photoionization cross-sections of he, ne, ar, kr, and xe, *Journal of Electron Spectroscopy and Related Phenomena* **123**, 265 (2002), determination of cross-sections and momentum profiles of atoms, molecules and condensed matter.
- [49] I. H. Suzuki and N. Saito, Absolute photoabsorption cross-sections of ne and xe in the sub-keV x-ray region, *Journal of Electron Spectroscopy and Related Phenomena* **129**, 71 (2003).
- [50] L. Zheng, M. Cui, Y. Zhao, J. Zhao, and K. Chen, Total photoionization cross-sections of ar and xe in the energy range of 2.1-6.0keV, *Journal of Electron Spectroscopy and Related Phenomena* **152**, 143 (2006).
- [51] J.-W. Chen, H.-C. Chi, C.-P. Liu, and C.-P. Wu, Low-energy electronic recoil in xenon detectors by solar neutrinos, *Phys. Lett. B* **774**, 656 (2017), arXiv:1610.04177 [hep-ex].
- [52] J. W. Cooper, Interaction of maxima in the absorption of soft x rays, *Phys. Rev. Lett.* **13**, 762

- (1964).
- [53] S. T. Manson and J. W. Cooper, Photo-Ionization in the Soft x-Ray Range: Z Dependence in a Central-Potential Model, *Phys. Rev.* **165**, 126 (1968).
 - [54] D. J. Kennedy and S. T. Manson, Photoionization of the noble gases: Cross sections and angular distributions, *Phys. Rev. A* **5**, 227 (1972).
 - [55] W. R. Johnson and K. T. Cheng, Photoionization of the outer shells of neon, argon, krypton, and xenon using the relativistic random-phase approximation, *Phys. Rev. A* **20**, 978 (1979).
 - [56] J.-W. Chen, H.-C. Chi, K.-N. Huang, C.-P. Liu, H.-T. Shiao, *et al.*, Atomic ionization of germanium by neutrinos from an ab initio approach, *Phys. Lett. B* **731**, 159 (2014), arXiv:1311.5294 [hep-ph].
 - [57] K. Freese, M. Lisanti, and C. Savage, Colloquium: Annual modulation of dark matter, *Rev. Mod. Phys.* **85**, 1561 (2013), arXiv:1209.3339 [astro-ph.CO].
 - [58] Atomic, molecular orbitals, and form factors on GitHub, <https://github.com/mccabech/AtMolDM>, gitHub repository.
 - [59] QEdark, <https://github.com/tientienyu/QEdark/>, gitHub repository.
 - [60] G. Anton *et al.* (EXO-200), Measurement of the scintillation and ionization response of liquid xenon at MeV energies in the EXO-200 experiment, *Phys. Rev. C* **101**, 065501 (2020), arXiv:1908.04128 [physics.ins-det].
 - [61] L. Baudis, P. Sanchez-Lucas, and K. Thieme, A measurement of the mean electronic excitation energy of liquid xenon, *Eur. Phys. J. C* **81**, 1060 (2021), arXiv:2109.07151 [physics.ins-det].
 - [62] J. Angle *et al.* (XENON10), A search for light dark matter in XENON10 data, *Phys. Rev. Lett.* **107**, 051301 (2011), [Erratum: *Phys.Rev.Lett.* 110, 249901 (2013)], arXiv:1104.3088 [astro-ph.CO].
 - [63] E. Aprile *et al.* (XENON), Low-mass dark matter search using ionization signals in XENON100, *Phys. Rev. D* **94**, 092001 (2016), [Erratum: *Phys.Rev.D* 95, 059901 (2017)], arXiv:1605.06262 [astro-ph.CO].